

Impact of Rare-earth site Substitution on the Structural, Magnetic and Thermal Properties of $Ce_{1-x}Eu_xCrO_3$ Orthochromite Solid-solutions

M. Taheri[†] and F. S. Razavi

Department of Physics, Brock University, St Catharines, ON, L2S 3A1, Canada

Z. Yamani and R. Flacau[‡]

Chalk River Nuclear Laboratories, Chalk River, ON, K0J 1J0, Canada

C. Ritter

Institut Laue-Langevin, F-38042 Grenoble, France

S. Bette and R. K. Kremer

Max Planck Institute for Solid State Research, Stuttgart, Germany

The role of slight changes of the chemical composition on antiferromagnetic ordering of Cr in rare-earth orthochromites was investigated on a series of ceramic solid-solutions $Ce_{1-x}Eu_xO_3$ where x varied from 0 to 1. Gradual replacement of Ce with Eu reduces the cell volume and acts equivalently to applying external pressure. Full replacement of Ce by Eu, on the other hand, reduces the Néel temperature from 260 K for $CeCrO_3$ to 178 K for $EuCrO_3$ as established by magnetization, heat capacity and neutron powder diffraction measurements. High resolution x-ray powder diffraction measurements on $Ce_{1-x}Eu_xO_3$ and neutron powder diffraction studies on $CeCrO_3$ enable to correlate the magnetic properties of the Cr magnetic subsystem with the size of the lattice and minute changes of the bonding and torsion angles within and between the CrO_6 octahedra. We find that the sizes and the shapes of the CrO_6 octahedra remain essentially unchanged as the size of the rare-earth cations is reduced whereas decreasing Cr - O - Cr bonding angles and increasing inclination of neighboring octahedra enable to compensate for the decreasing lattice size.

PACS numbers: 75.25.-j, 75.47.Lx, 65.40.Ba, 65.40.De, 75.50.Ee

I. INTRODUCTION

Rare-earth orthochromites which crystallize with the orthorhombic $GdFeO_3$ structure-type (Figure 1) have attracted special attention, because they may exhibit ferroelectric polarization either induced by an external magnetic field or spontaneous polarization due to internal magnetic fields induced by long-range magnetic ordering.¹⁻⁶ For example, magneto-electric effects as well as magnetic and electric field induced switching of the dielectric polarization have been detected in $SmCrO_3$, $GdCrO_3$, and $ErCrO_3$.² Still controversial is the relevance of the interaction between the rare-earth magnetism and the weak ferromagnetism due to spin canting in the Cr subsystem. For example, polarization in $ErCrO_3$ vanishes at a spin re-orientation transition at ~ 22 K below which spin canting of the Cr moments also disappears emphasizing the importance of weak ferromagnetism and the interaction with the rare-earth subsystem for polar ordering.² For $LuCrO_3$, on the other hand, Preethi Meher *et al.* observed qualitatively similar ferroelectric-like characteristics as in $ErCrO_3$, though weaker in magnitude, revealing that orthochromites with a diamagnetic rare-earth constituent can also develop a polar state questioning the necessity of rare-earth magnetism for establishing multiferroicity in the orthochromites.⁵ At present, there are also diverging conclusions as to whether the multiferroic state as

evidenced by polarization and pyroelectric currents occurs below the Néel temperature² or whether it is already formed at higher temperatures.^{1,7} Ghosh *et al.* have observed that in $SmCrO_3$ and $HoCrO_3$ polar order already develops in the paramagnetic state and they attributed this observation to a structural transition from the centrosymmetric orthorhombic space group $Pbnm$ to the non-centrosymmetric space group $Pna2_1$.^{8,9} Kumar *et al.*¹⁰ recently, suggested that an additional driving force for observation of ferroelectricity in rare-earth orthochromites is the short range exchange interactions.¹¹

The range of the magnetic ordering temperatures of the $RCrO_3$ opens up potential applications for these compounds. Compared to what has been observed, for example, in the orthomanganites family, $RMnO_3$, (e.g. $T_N \sim 27$ K in $TbMnO_3$) which comprises some of the most prominent multiferroic systems, the rare-earth orthochromites exhibit ordering temperatures close to room temperature. Also, since the coupling between the $4f$ and the $3d$ electrons in the half filled t_{2g} orbitals of the Cr^{3+} cations can be large, orthochromites may have some advantages compared to orthoferrites. Although the latter exhibit higher magnetic ordering temperatures, Cr^{3+} lacks fourth order crystal field splitting terms acting on the $S = \frac{3}{2}$ spin multiplet (cf. Ref. 13). This might allow higher complexity of spin canting and spin reorientation phenomena in the magnetic structures of the rare-earth orthochromites.

The structural and magnetic properties of the rare-

earth orthochromites, RCrO_3 , have been studied in some detail before.^{12,14–16} By using high-resolution neutron powder diffraction, Zhou *et al.* determined the crystal structures including the oxygen atom positions with great precision.¹² They found that the cooperative rotation and tilting of the CrO_6 octahedra essentially tunes the $t_{2g} - e_g$ overlap and the Cr - O - Cr superexchange which can explain the sizeable decrease of the Néel temperature when substituting smaller rare-earth cations. The Néel temperature, T_N , of the Cr substructure which is at about 300 K for LaCrO_3 decreases monotonically as the rare-earth element is replaced by a heavier one with T_N for LuCrO_3 of about 100 K.¹⁴ CeCrO_3 , studied by Shukla *et al.*, exhibits a Néel temperature of ~ 260 K close to that of LaCrO_3 .¹⁵ EuCrO_3 orders at ~ 178 K with a slightly canted antiferromagnetic structure.¹⁶

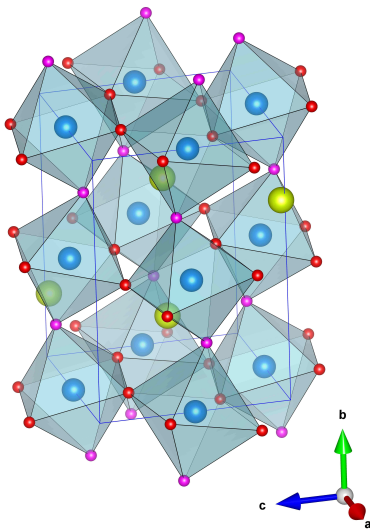


FIG. 1. (color online) Crystal structure of $(\text{Ce,Eu})\text{CrO}_3$ in space group $Pnma$ (no. 62). Yellow/green and blue spheres represent cerium/europium and chromium atoms, respectively. The O2 atoms connecting the CrO_6 octahedra in the $a - c$ plane are given by red spheres and the O1 atoms connecting along b are represented by magenta spheres. A unit cell is outlined.

The marked decrease of the Néel temperature of the Cr substructure in the series from the light to the heavy rare-earth elements with the simultaneous reduction of the unit cell volume already were suggestive that the Cr - Cr distances alone cannot be the determining factor for the Cr magnetic ordering in the RCrO_3 . Rather, as concluded by Zhou *et al.* bonding and tilting angles of the CrO_6 octahedra change and the crystal structure becomes more distorted, reducing Cr - O - Cr electron transfer and in turn superexchange between the Cr cations.¹² Bhadram *et al.* have investigated the variation of the room temperature lattice parameters and Raman frequencies of RCrO_3 ($\text{R} = \text{Eu, Gd, Tb, Lu}$) with pressure and found that the octahedral tilts decrease linearly with increasing R radii.¹⁷ Compressibility increases for small R ions whereas the structures of rare-earth or-

thochromites with larger R ions are stiffer. They concluded that for the Néel temperature the Cr - O bond lengths play a dominant role over the octahedral tilts.¹⁷ Zhao *et al.* using first-principles calculations found opposite dependence of the Néel temperature on hydrostatic or chemical pressure.¹⁸ Whereas, hydrostatic pressure increases the Néel temperature chemical pressure e.g. induced by replacing larger rare-earth cations by smaller ones lowers the Néel temperature, in qualitative agreement with the Néel temperatures observed across the series of the rare-earth orthochromites.

For CeCrO_3 ($T_N \sim 260$ K) Shukla *et al.* found a G -type magnetic ordering of the Cr substructure and also proposed ordering of the Ce moments below ~ 100 K and a spin re-orientation below ~ 15 K. However, this conclusion was based on very faint additional magnetic scattering peak in the neutron powder diffraction patterns at temperatures well below ~ 100 K.¹⁵ The refined Ce moments amounted to $\sim 0.7 \mu_B$ and pointed antiparallel to the Cr moments. In preceding publications, we have investigated in detail the magnetic properties of EuCrO_3 and CeCrO_3 .^{16,20} Below 178 K, the Cr substructure in EuCrO_3 orders with a G_x -type antiferromagnetic structure with an ordered moment of $\sim 2.4 \mu_B$, consistent with the $S = \frac{3}{2}$ spin-only ground state. A weak canted ferromagnetic moment pointing along the c -axis ($Pbnm$ notation) could be concluded from the neutron diffraction investigation. It amounts to $\sim 0.1 \mu_B$, consistent with single crystal magnetization data.²² Evidence for ordering of the Eu moments has neither been found in the neutron powder diffraction data nor in the heat capacity or magnetization data. This observation can be understood as being due to the $J = 0$ Hund's rule ground state and the van Vleck-type temperature dependent moment of the Eu^{3+} cations.¹⁶ In contrast to the absence of conclusive evidence for R moment ordering in CeCrO_3 and EuCrO_3 , there is some unusual behavior of the magnetic susceptibilities at low temperature.^{15,20} Especially, the field-cooled (FC) susceptibility of CeCrO_3 showed a compensation point at ~ 50 K with negative magnetization below. Irrespective of the measuring field, zero-field cooled (ZFC) and FC magnetic susceptibilities intersected at ~ 100 K with the FC susceptibility being smaller than the ZFC susceptibility. This complex behavior could be due to inhomogeneity in the small sample grains (typically < 100 nm, "core-shell" behavior) or be due to some complex compensation of R and Cr moments induced by external fields.²⁰

We explore in this paper the changes of the magnetic and structural properties induced by the replacement of a larger rare-earth cation Ce^{3+} by the smaller one Eu^{3+} with ionic radii of 1.283 Å and 1.144 Å, respectively.²¹ Especially, we study in detail the changes of the crystal structure and magnetic properties in small steps with a series of solid-solutions of CeCrO_3 and EuCrO_3 , the latter having unit cell volumes of 230.8 Å³ and 224.8 Å³, respectively. Gradual replacement of Ce with Eu leads to an increase of the cell distortion factor¹⁹ by $\sim 50\%$

similar to the effect of external hydrostatic pressure of ~ 10 GPa or more.¹⁷ On the other hand, EuCrO_3 has a markedly lower Néel temperature than CeCrO_3 suggesting that substituting Ce by the smaller Eu cations i.e. chemical pressure will act differently from hydrostatic pressure, supporting the first-principles results obtained by Zhao *et al.*¹⁸

The paper is organized in two parts, followed by a summary: We first describe structural properties of the $\text{Ce}_{1-x}\text{Eu}_x\text{CrO}_3$ phases across the entire solid-solution range $0 \leq x \leq 1$. This set of solid-solutions allows to tune the mean ionic radius of the rare-earth cations between those of Ce and Eu, thus covering continuously a range which was accessed by high-resolution neutron powder diffraction for NdCrO_3 and PrCrO_3 only. Samples containing Sm, Eu, and Gd orthochromites were not included in this series.¹² In the second part, we present the results of our temperature, field and thermal history dependent of dc and ac magnetic susceptibilities and thermal properties and report first neutron powder diffraction investigations on the solid solutions $\text{Ce}_{1-x}\text{Eu}_x\text{CrO}_3$. Finally, we discuss the results and summarize.

II. EXPERIMENT

Powder samples of $\text{Ce}_{1-x}\text{Eu}_x\text{CrO}_3$ were synthesized by the solution combustion method starting from equimolar solutions of high purity cerium and europium nitrate, chromium nitrate and glycine as described in detail elsewhere.^{20,23} The products were characterized with respect to phase purity by x-ray powder diffraction (XRPD) at room temperature using $\text{MoK}\alpha_1$ radiation ($2\theta_{max} \sim 110^\circ$, STOE triple DECTRIS MULTIMYTHEN silicon strip detector). Neutron powder diffraction (NPD) patterns of CeCrO_3 were collected at room temperature on the high-resolution two-axis diffractometer D2B installed at the Institut Laue-Langevin (ILL, Grenoble) using neutrons of 1.594 Å wavelength. The polycrystalline sample of ~ 9 g was contained in a thin-walled vanadium container of 8 mm outer diameter. Rietveld refinements by varying lattice parameters and atom positions were performed in the orthorhombic spacegroup $Pnma$ (no. 62) using the *FullProf* or the TOPAS software²⁴⁻²⁶ assuming a Thompson-Cox-Hastings pseudo-Voigt peak profile (*FullProf* NPR = 7). Isotropic and anisotropic displacement parameters were tested in case of the x-ray and neutron diffraction patterns, respectively. Since marked anisotropies could not be seen we report isotropic displacement parameters in the following. The background was modeled by a higher-order Chebychev polynomial. The refinements typically converged to Bragg- and R_f-reliability factors of $\sim 2\%$ or less and χ^2 -values better than 1 were achieved for the x-ray patterns. For the neutron diffraction pattern of CeCrO_3 , the reliability factors were somewhat larger (see Table I). Medium resolution high intensity neutron scattering was performed on the N5

triple axis spectrometer at the Chalk River Laboratories in order to follow the temperature dependence of magnetic Bragg peaks. Initial and final neutron energies were chosen by the pyrolytic graphite PG002 reflections. In order to reduce the high absorption cross section for thermal neutrons from the ^{151}Eu isotope in the natural isotope composition of Eu, the samples with a Eu content larger than 10% were contained in flat geometry thin-walled aluminum sample holders which were long enough to cover the full beam height, but reduced the thickness of the sample to ~ 1 mm.²⁷ dc magnetization were measured using a Magnetic Property Measurement System (Quantum Design, MPMS). Heat capacity measurements were performed on compressed pellets in a Physical Property Measurement System (Quantum Design, PPMS). The particle size of the powders was determined with a Hitachi H-7650 transmission electron microscopy (TEM) and a Zeiss Sigma VP scanning electron microscopy (SEM) equipped with the Oxford Inca EDX.

III. RESULTS

A. Chemical and Structural Characterization

Chemical and structural properties and the morphology of the boundary phases CeCrO_3 and EuCrO_3 as well as a surface analysis of the $\text{Ce}_{1-x}\text{Eu}_x\text{CrO}_3$ nano-powders have been described in detail elsewhere.^{16,20,23,28} Figure 2 summarizes typical result of our EDX microprobe analysis and the TEM picture of the sample $\text{Ce}_{0.9}\text{Eu}_{0.1}\text{CrO}_3$. A statistical analysis of the sample grain sizes indicated a Gaussian distribution with a maximum at ~ 75 nm and a FWHM of ~ 50 nm, similar to what has been reported for pure CeCrO_3 and EuCrO_3 .^{16,20,23}

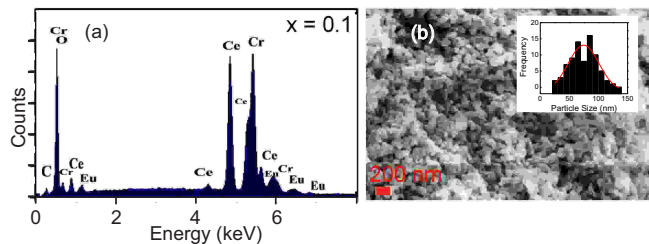


FIG. 2. (color online) (a) EDX diagram of the phase $\text{Ce}_{0.9}\text{Eu}_{0.1}\text{CrO}_3$. (b) TEM image with corresponding size distribution histogram (inset) of the same sample. The red solid line is a Gaussian centered at ~ 75 nm and a FWHM of ~ 50 nm.

The results of our NPD on CeCrO_3 and the XRPD experiments on $\text{Ce}_{1-x}\text{Eu}_x\text{CrO}_3$ together with the Rietveld refinements are shown in Figures 3 and 4(a-c). The comparison of the refined structural parameters compiled in Table I reveals good agreement between parameters refined from our XRPD and NPD patterns and previously reported data.¹⁵ Merely some atom positional parameters of the two oxygen atoms O1 (Wyckoff site 4c) and

O2 (Wyckoff site $8d$) differ slightly which also explains the small differences in the Cr - O - bonding angles. The angle α which reflects the O21 - Cr - O22 bonding angle in the equatorial plane of the CrO_6 octahedra and the angle β which measures the tilt of the Cr - O1 direction with respect to the plane spanned by the O2 atoms and the Cr atoms are very close to 90° and less different and agree well for both techniques and previously published data.¹⁵ The characteristic Cr - O distances and O - Cr - O bonding angles are compiled in Table II.

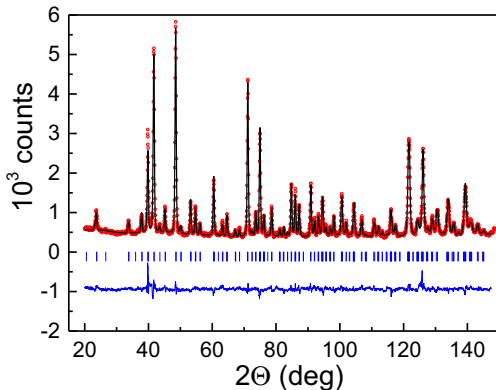


FIG. 3. (color online) The NPD patterns of CeCrO_3 collected at room-temperature using neutrons with a wavelength of $\lambda = 1.594 \text{ \AA}$. Black circles represent the measured data, the red solid line is the calculated pattern of the Rietveld refinement. The blue solid line at the bottom of the graph shows the difference between the observed and calculated patterns. Vertical ticks (blue) mark the position of the Bragg reflections used to simulate the refined patterns.

The high absorption cross section of the element Eu with the natural isotope composition usually prevents high-resolution NPD measurements on Eu substituted samples. In order to follow the variation of the crystal structure and especially the shifts of the oxygen atoms of Eu substituted samples, $\text{Ce}_{1-x}\text{Eu}_x\text{CrO}_3$, we therefore used the lattice and positional parameters determined from the refinement of the XRPD patterns. The XRPD patterns of a total of nine phases of $\text{Ce}_{1-x}\text{Eu}_x\text{CrO}_3$ ($0 \leq x \leq 1$) and that of GdCrO_3 were measured and Rietveld refinements were performed. Fig. 4(a - c) displays three characteristic diffraction patterns covering the entire range of x compared with the results of the refinements and the difference between observed and calculated patterns. In addition to the lattice parameters and the atom positions shown in the following figures (cf. Fig. 5 - 8), background and displacement parameters have also been refined which will not be discussed any further.

Fig. 5 summarizes the lattice parameters and the cell volume of the phases $\text{Ce}_{1-x}\text{Eu}_x\text{CrO}_3$ versus the Eu content. The cell volume decrease linearly with a magnitude which is in good agreement with previous findings.¹⁴ Whereas a and c follow a Vegard's-law with a linear de-

TABLE I. Structural parameters and conventional reliability factors as obtained from Rietveld profile refinements of our XRPD and NPD patterns collected at 295 K with Mo- $K_{\alpha 1}$ radiation and neutrons with a wavelength of $\lambda = 1.549 \text{ \AA}$ on CeCrO_3 . The Rietveld refinements were performed assuming the space group $Pnma$ (no. 62). The respective site occupancies were not refined from the XRPD pattern whereas the refinement of the NPD pattern indicated full occupation as of the oxygen sites. Data by Shukla *et al.*¹⁵ are given in the rightmost column.

T (K)	295 (XRPD)	295 K (NPD)	300 K (NPD) ¹⁵
a (\AA)	5.4736(1)	5.4729(2)	5.472(1)
b (\AA)	7.7311(1)	7.7304(3)	7.733(1)
c (\AA)	5.4818(1)	5.4808(2)	5.479(1)
V (\AA^3)	231.97(1)	231.88(2)	231.84(11)
Ce (4c)			
x	0.5280(1)	0.5272(6)	0.5294(20)
y	1/4	1/4	1/4
z	0.5050(2)	0.5046(2)	0.5054(9)
B_{iso} (\AA^2)	0.35(1)	0.32(1)	0.5
Cr (4b)			
x	0	0	0
y	0	0	0
z	1/2	1/2	1/2
B_{iso} (\AA^2)	0.24(1)	0.23(1)	0.5
O1 (4c)			
x	0.9856(7)	0.9902(7)	0.9948(15)
y	1/4	1/4	1/4
z	0.4220(15)	0.4304(7)	0.4260(14)
B_{iso} (\AA^2)	0.23(5)	0.24(1)	0.9
O2 (8d)			
x	0.2831(9)	0.2834(4)	0.2821(7)
y	0.0358(7)	0.0391(3)	0.0389(6)
z	7192(9)	0.7146(5)	0.7201(8)
B_{iso} (\AA^2)	0.23(5)	0.29(1)	0.9
Bragg R-factor (%)	1.54	3.94	
R_f -factor (%)	1.86	2.96	

TABLE II. Interatomic distances and bonding angles of CeCrO_3 calculated from the parameters given in Table I. The angles α and β are defined as the O21 - Cr - O22 bonding angle in the midsection of the CrO_6 octahedra and the torsion angle β is given by the tilt of the Cr - O1 direction with respect to a neighboring Cr - O1 bonds.

	XRPD	NPD
Cr - O21 (\AA)	1.964(5)	1.969(3)
Cr - O22 (\AA)	1.980(5)	1.986(3)
Cr - O1 (\AA)	1.981(2)	1.9706(8)
α ($^\circ$)	88.72(16)	88.65 (11)
β ($^\circ$)	89.61(5)	89.25(4)
\angle O1 - Cr - Cr - O1 ($^\circ$)	15.61(4)	16.7(4)
\angle Cr - O2 - Cr ($^\circ$)	158.2(3)	156.50(15)

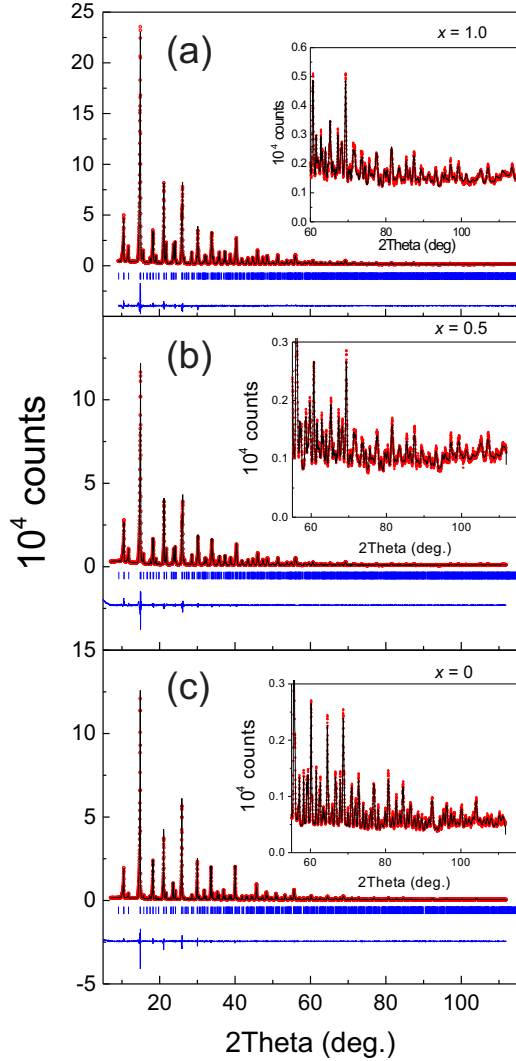


FIG. 4. (color online) The XRPD patterns of $\text{Ce}_{1-x}\text{Eu}_x\text{CrO}_3$ ($x = 0.0, 0.5, 1.0$, from bottom to top) collected at room-temperature with $\lambda = 0.709319\text{\AA}$ (Mo $\text{K}_{\alpha 1}$). Black circles represent the measured data, the red solid line is the result of the Rietveld refinement. The blue solid line at the bottom of the graph shows the difference between the observed and calculated patterns. Vertical ticks (blue) mark angles of the Bragg reflections used to simulate the refined patterns.

pendence on x , b exhibits non-linear behavior with a bending away from a linear relationship towards large x . Remarkable is also the crossing of the lattice parameters a and c at $x \sim 0.04$ (see inset Figure 5) which similarly has been reported by Prado-Gonjal *et al.* to lie between LaCrO_3 and PrCrO_3 .¹⁴

The cell distortion factor, d , introduced by Sasaki *et al.* to measure the deviation of distorted perovskite-type structures from cubic symmetry is estimated according to¹⁹

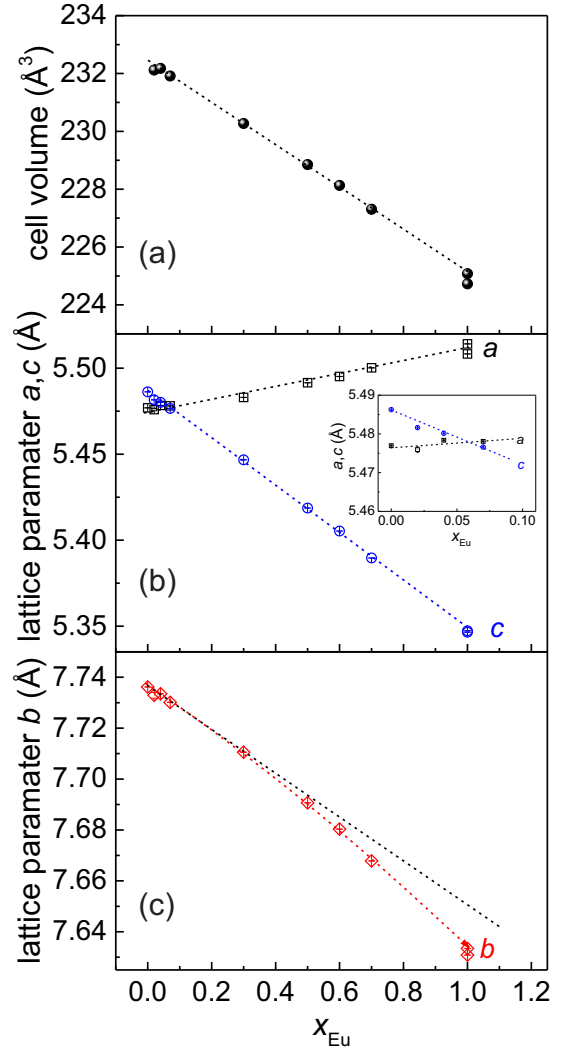


FIG. 5. (color online) (a) Cell volume and lattice parameters a , b and c versus the Eu content x for the phases $\text{Ce}_{1-x}\text{Eu}_x\text{CrO}_3$ ($Pnma$ setting). The inset shows the crossing of the lattice parameters a and c for small x . The colored dashed lines are guides to the eye. The black dashed line in (c) emphasizes the non-Vegard's behavior of the lattice parameter c .

$$d = 10^6 \times (a/\sqrt{2} - a_p)^2 + (b/2 - a_p)^2 + (c/\sqrt{2} - a_p)^2 / a_p^2 / 3, \quad (1)$$

where the average 'cubic' lattice parameter a_p is given by

$$a_p = (a/\sqrt{2} + b/2 + c/\sqrt{2})/3. \quad (2)$$

d shows a maximum distortion of ~ 150 ppm for EuCrO_3 (cf. Fig. 6), whereas for CeCrO_3 d almost vanishes. Compared to the high pressure data by Venkata *et al.*²⁹ a cell distortion factor of 150 ppm is comparable to distortion factors obtained for example in EuCrO_3

for pressures of ~ 10 GPa. Remarkable is the negative slope of the distortion factor, for small, values of $x \leq 0.04$ below the intersection of the lattice parameters a and c (cf. inset Fig. 6) paralleling the crossing of the lattice parameters a and c in this concentration range.

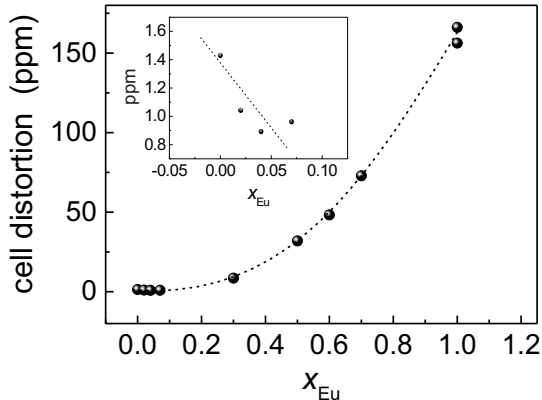


FIG. 6. (color online) Cell distortion factor for $Ce_{1-x}Eu_xCrO_3$ calculated according to Eq. (1).

The gradual replacement of the larger Ce^{3+} cations by the smaller Eu^{3+} cations leads to systematic shifts of the atoms in the crystal structures of the phases $Ce_{1-x}Eu_xCrO_3$ with about the same magnitude for all atoms involved (R, O1, and O2). Figure 7 summarizes our results for the R and the O1 positional parameters. The z and x coordinates of the Ce/Eu atoms are linearly related. Both are slightly decreasing with a growing Eu content. In the inset to Fig. 7(a), we highlight a projection of the crystal structure of $Ce_{1-x}Eu_xCrO_3$ along $[010]$ with arrows representing the atom shifts resulting from a 80% replacement ($x = 0.8$) of Ce by Eu cations. The Ce/Eu atoms move in the $a - c$ plane away from the symmetric $(1/2, 1/4, 1/2)$ position with the movement along $\langle 100 \rangle$ being somewhat more pronounced. In contrast to the R atoms, the tilting of the apical oxygen atoms O1 away from $\langle 010 \rangle$ with an increasing Eu content is more complex: As revealed by a plot of the coordinate z_{O1} versus x_{O1} the movement of the O1 atoms splits into two separate branches with a significantly different dependence on x . For a small Eu content ($x < 0.04$) z_{O1} is almost independent of x_{O1} , whereas for ($x > 0.04$) one observes a linear relationship of z_{O1} versus x_{O1} which reflects a correlated tilting of the CrO_6 octahedra into the $a - c$ plane away from a stretched configuration.

The apical oxygen atoms O1 move only slightly away from a orthogonal orientation with respect to the Cr - O2 equatorial plane in the CrO_6 octahedra. Figure 8 shows a maximum "skewness" of less than 2° with an opposite movement of $\angle (O22 - Cr - O1)$ and $\angle (O21 - Cr - O1)$ around an average value of ~ 90 deg. This tilting of the CrO_6 octahedra leads to an increased torsion of neighboring CrO_6 octahedra with respect to each

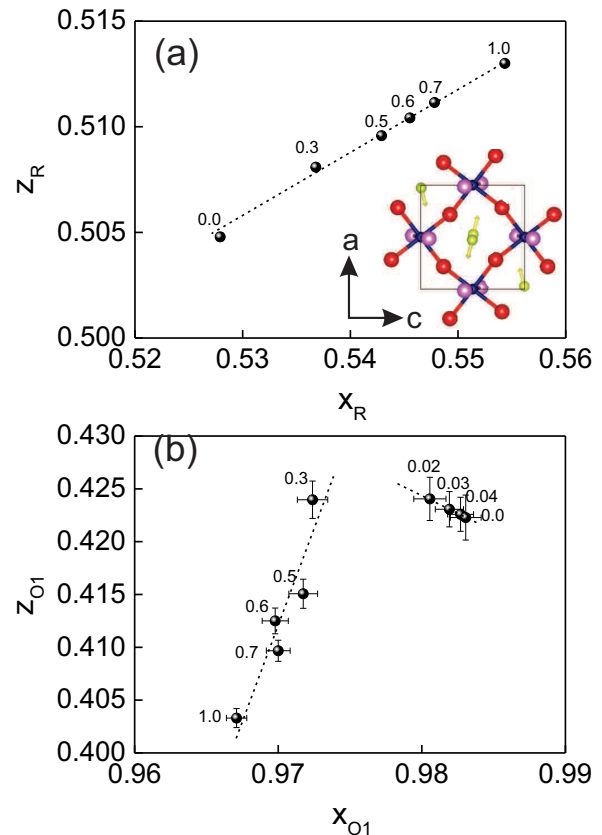


FIG. 7. (color online) (a) Atom positional parameters of the R atoms versus the Eu content (x) for the $Ce_{1-x}Eu_xCrO_3$ phases. Error bars are of the size of points. The inset highlights a projection of the crystal structure along $[010]$ with arrows representing the shifts of the R atoms in the crystal structure initiated by the replacement of 80% of the Ce by Eu atoms, i.e. by comparing phases with $x = 0$ and $x = 0.8$. The length of the arrows is proportional to the atom shifts. (b) Atom positional parameters z_{O1} , x_{O1} of the apical oxygen atoms O1 in the CrO_6 octahedra. The (black) dashed lines are guides to the eye. The numerals give the Eu content x .

other (cf. Figure 9(b)). The torsion angle O1 - Cr - Cr - O1 exhibits a linear dependence on the Eu content and increases markedly by about 22%. The torsion angle is linearly correlated with the Cr - O2 - Cr bonding angle (cf. Figure 9(c)). The latter characterizes the opposite movement of the O2 equatorial oxygen atoms outward and inward away from a 180° Cr - O - Cr bond as displayed in Fig. 9(a).

Figure 10 summarizes the Cr - O distances in the CrO_6 octahedra. The Cr - O2 distances (Cr - O21 and Cr - O22, i.e. the distance to the O atoms which lie essentially in the $a - c$ plane in $Pnma$ setting) exhibit an opposed x dependence with about the same magnitude of the slopes. The Cr - O1 distance to the apical oxygen atoms essentially parallel b undergoes a moderate elongation. An estimation of the octahedral distortion factor which we defined in analogy of the cell distortion factor according

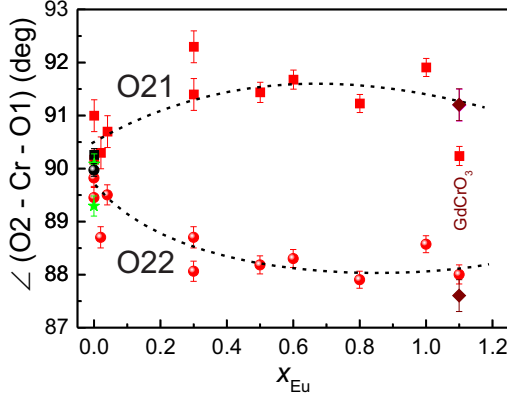


FIG. 8. (color online) O2 - Cr - O1 angles derived from our neutron diffraction data (black circles and squares) and the x-ray diffraction (red circles and squares) measurements. Dashed lines are guides to the eye. Literature data are also plotted: (green) asterisks CeCrO_3 ¹⁵; (brown) diamond GdCrO_3 ³³.

to

$$d_{\text{oct}} = \frac{1}{6} \sum_{i=1}^6 (d_{i\text{Cr-O}} - d_{\text{ave}})^2, \quad (3)$$

where the mean distance, d_{ave} is calculated from the six Cr to oxygen distances in the CrO_6 octahedra, and $d_{i\text{Cr-O}}$, using

$$d_{\text{ave}} = \frac{1}{6} \sum_{i=1}^6 d_{i\text{Cr-O}}, \quad (4)$$

indicates an octahedral distortion between 5 and 10 ppm (cf. Figure 10(d)), largely independent of the Eu content.

B. Magnetic Properties

The temperature dependence of the dc magnetizations in an applied magnetic field of $\mu_0 H = 0.05$ T of several polycrystalline samples of $\text{Ce}_{1-x}\text{Eu}_x\text{CrO}_3$ was measured in a warming cycle after the samples had been slowly cooled (~ 1.5 K/min) either with zero field (ZFC) or magnetic field (FC). The ZFC and FC data summarized in Figure 11 reveal an antiferromagnetic ordering of the Cr moments. The Néel temperature decreases from 260 K (CeCrO_3) to 178 K (EuCrO_3). Small peaks are seen in the ZFC traces whereas the FC magnetizations exhibit a sharp increase reminiscent of the built-up of spontaneous magnetization in a ferro- or ferrimagnet. These anomalies become more pronounced with increasing Eu content x . In addition, the ZFC magnetizations show maxima

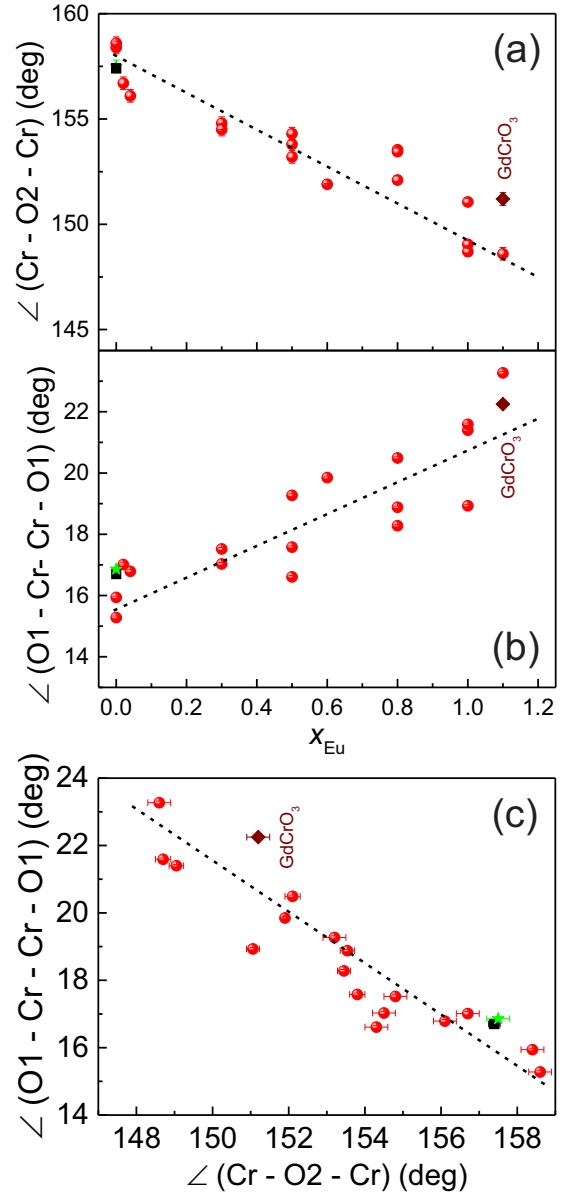


FIG. 9. (color online) (a) Cr - O2 - Cr bonding angles versus Eu content. Plotted is the bonding angle away from a line connecting two Cr atoms. (b) Torsion angle O1 - Cr - Cr - O1. (c) Torsion angle of (a) versus bonding angle shown in (b). Bonding angles calculated from literature data are also plotted: (green) asterisk: CeCrO_3 ¹⁵; (brown) diamond: GdCrO_3 ³³.

below ~ 70 K, especially for smaller Eu contents ($x < 0.5$) and negative magnetization which is attributed to the development of rare-earth magnetic ordering. The inset in Figure 11(a) shows, for example, the ZFC (blue solid line) and the FC (red solid line) susceptibilities of CeCrO_3 ($x = 0.0$) which bifurcate from each other at a splitting temperature of ~ 258 K. By warming up from 1.8 K to room temperature, $\chi(\text{ZFC})$ decreases gradu-

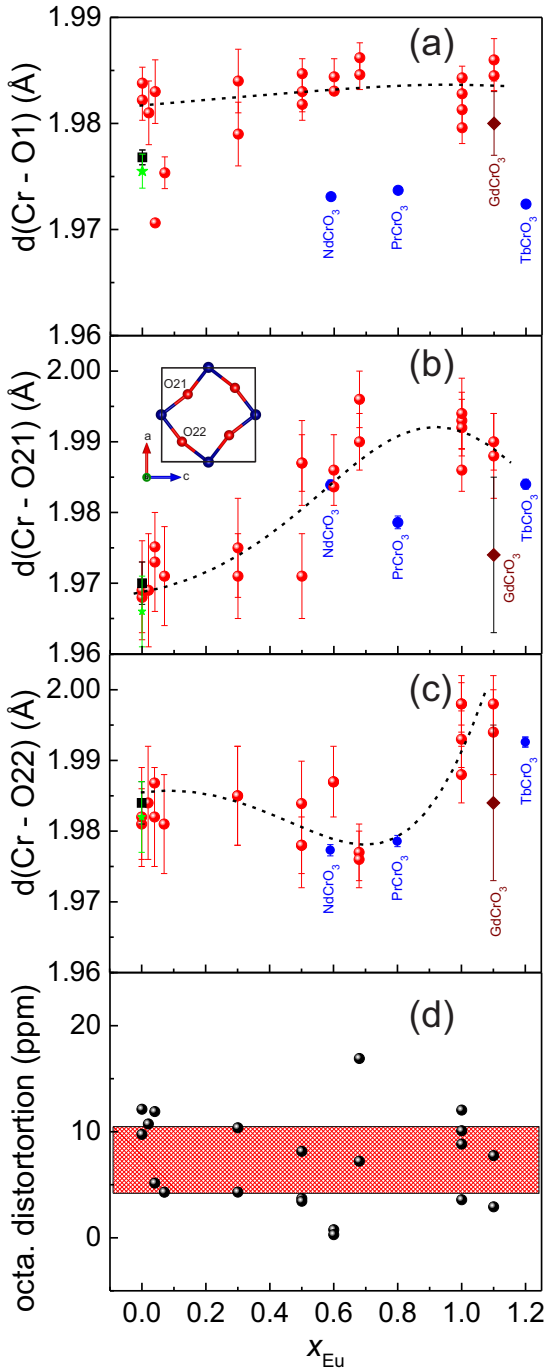


FIG. 10. (color online) (a - c) (black) square Cr-to-oxygen interatomic distances derived from our neutron powder diffraction data and the x-ray diffraction (red) circles patterns. Dashed lines are guides to the eye. The upper left inset in (b) gives the assignment of the O21 and O22 atoms. Octahedral distortion factor according to Eq. (3). Literature data are also plotted: (blue) circles RCrO_3 ($R = \text{Nd, Pr, Tb}$)¹², (green) asterisk CeCrO_3 ¹⁵; (brown) diamond GdCrO_3 ³³. (d) The octahedral distortion factor calculated from the distances in (a) - (c) according to Eq. (3). The dashed area indicates an interval of 3σ around an mean value of 7.5 ± 0.9 .

ally until it reaches the transition temperature at $T_N \sim 260$ K in good agreement with previous studies on orthochromites.^{15,30-32} $\chi(\text{ZFC})$ is positive at all temperatures, whereas in FC measurements the susceptibility (red line) increases up to the transition temperature of $T_1 \sim 12$ K and then decreases again to become zero at the compensation temperature, T_{comp} . Below T_{comp} , the magnetization is negative while with further warming, it changes back to positive values. Above T_{comp} , the magnetization increases to attain a maximum at $T_b \sim 220$ K and then decreases gradually to reach the transition temperature $T_N \sim 260$ K. The T_1 anomaly may be ascribed to the magnetic ordering of cerium ions which similarly has been seen as the spin reorientation in different members of RCrO_3 compounds^{15,34,35}. Interestingly, Ce ordering appears to have no immediate impact on the Cr magnetic structure as the intensity of the (110)/(011) magnetic Bragg reflection follows an standard order parameter temperature dependence (see discussion and Figure 13 below).

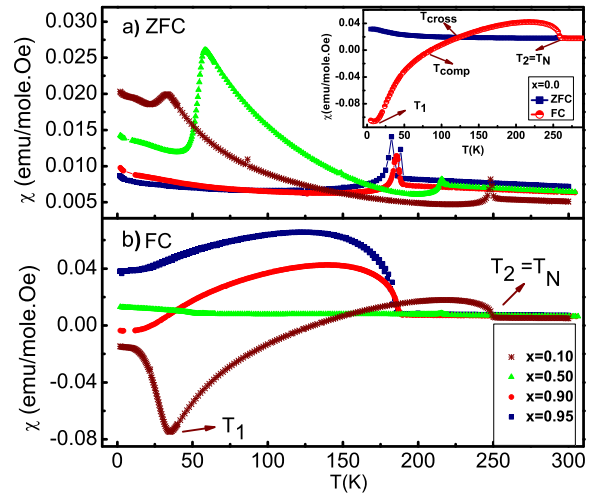


FIG. 11. (online color) (a) ZFC and (b) FC susceptibilities versus temperature of polycrystalline samples of $\text{Ce}_{1-x}\text{Eu}_x\text{CrO}_3$ ($x = 0.1, 0.5, 0.9$ and 0.95) under an applied magnetic field of 500 Oe. The inset in (a) shows the temperature dependence of ZFC and FC susceptibilities of CeCrO_3 .

C. Heat Capacities

The heat capacities of most rare-earth orthochromites, RCrO_3 ($R = \text{La, Pr, Nd, Sm, Gd, Dy, Ho, Er}$ and Y) have been reported by Satoh *et al.*³⁶, Bartolomé *et al.* and Su *et al.*³⁷⁻³⁹ In this work, we measured the heat capacities on $\text{Ce}_{1-x}\text{Eu}_x\text{CrO}_3$ phases down to liquid helium temperature at zero magnetic field and studied the anomalies associated with the long-range magnetic ordering of Cr^{3+} ions. Figure 12 displays the temperature dependence of the heat capacity of the $\text{Ce}_{1-x}\text{Eu}_x\text{CrO}_3$ from 1.8 K to 300 K in zero magnetic field where $x =$

0.0, 0.2, 0.4, 1.0. The long-range ordering of the Cr^{3+} moments indicated by the λ -shaped anomaly shifts from 256 K for $x = 0.0$ to 175 K for $x = 1.0$. Especially for small Eu contents, the heat capacities at low temperatures revealed additional magnetic contributions. These can be clearly separated from the total heat capacities when the heat capacities of the lattice were subtracted. The lattice heat capacities were estimated from the data of the non-magnetic isotypic polycrystalline sample^{16,23} of LaGaO_3 by scaling the temperature according to the different molar masses of RCrO_3 and LaGaO_3 following the procedure proposed by Bouvier *et al.*⁴⁰

The magnetic entropy of CeCrO_3 gained by integrating C_{mag}/T vs. T , is plotted in the inset in Figure 12. At low temperatures, the entropy amounts to $\sim R \ln 2$ indicating a doublet crystal field ground state of Ce^{3+} . Towards higher temperatures, the entropy captures contributions from excited crystal field states of Ce^{3+} and contributions of Cr^{3+} moment ordering. At the Néel temperature, the entropy reaches a value of $\sim R \ln 4$.

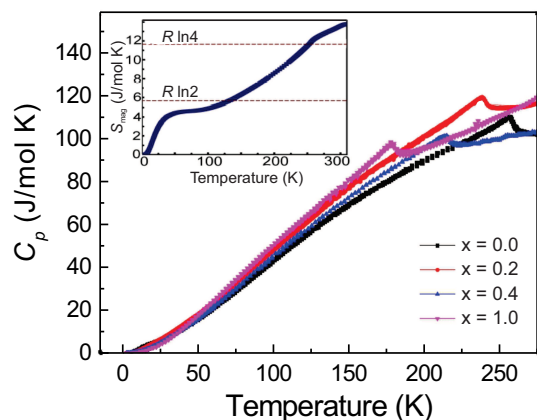


FIG. 12. (color online) Temperature dependence of total heat capacities of $\text{Ce}_{1-x}\text{Eu}_x\text{CrO}_3$ ($x = 0.0, 0.2, 0.5, 1.0$). The inset shows the temperature dependence of magnetic entropy of CeCrO_3 ($x = 0.0$).

D. Magnetic Neutron Scattering

In order to determine the exact values of T_N , temperature dependent low-resolution high-intensity neutron powder diffraction patterns was carried out on several samples of $\text{Ce}_{1-x}\text{Eu}_x\text{CrO}_3$. Below the Néel temperature, all patterns exhibited a pronounced magnetic Bragg reflection near $2\theta \sim 30.9^\circ$ which can be indexed as (110)/(011). Additional, apparent magnetic scattering intensity was noticed for the (211)/(031) similar to what has been reported for CeCrO_3 by Shukla *et al.* before.¹⁵ The integrated intensities of the (110)/(011) magnetic Bragg reflection are compiled in Figure 13.

The integrated intensities follow a typical temperature dependence with saturation at low temperatures. Near to T_N the temperature dependence of the intensities for CeCrO_3 was fitted to a critical power law $((T_N - T)/T_N)^{2\beta}$ as shown in the inset to Figure 13 resulting in critical exponents, β , close to 0.34 in agreement with values expected for typical 3dim universality classes. None of the temperature traces for the different compositions reveals any signatures for re-orientation of the Cr moments at low temperatures associated to the anomalies observed in the magnetic susceptibilities (cf. Figure ref-SuceptZ(FC) indicating weak exchange coupling between the Ce moments. These rather orient readily in a stronger exchange fields of the Cr moments without a feed back.

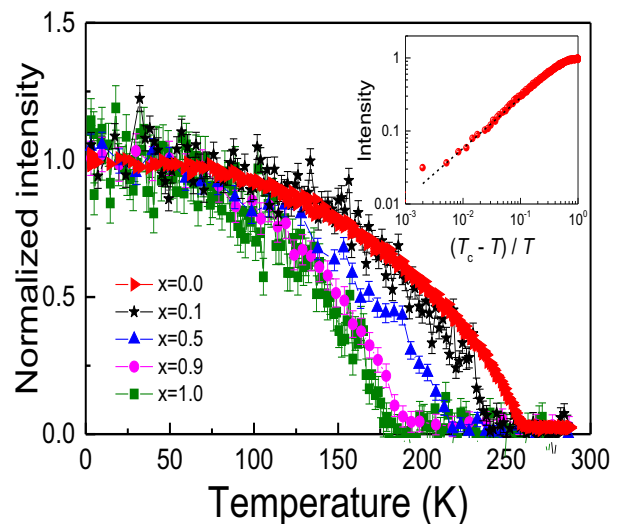


FIG. 13. (online color) Integrated intensity of the (110)/(011) magnetic Bragg reflection at $2\theta \sim 30.9^\circ$ vs temperature for various samples of $\text{Ce}_{1-x}\text{Eu}_x\text{CrO}_3$ as indicated. The inset shows the intensity versus the reduced temperature, $t = (T_N - T)/T_N$, where the critical temperature, T_N , for CeCrO_3 amounts to 258.1(1) K. The dashed line represents a critical power law $\propto t^{2\beta}$ with a critical exponent $\beta = 0.346(5)$.

IV. DISCUSSION AND SUMMARY

We have synthesized high-purity ceramic samples of $\text{Ce}_{1-x}\text{Eu}_x\text{O}_3$ where x varied from 0 to 1. Extensive studies of the structural parameters by neutron and x-ray powder diffraction measurements reveal the dependence of antiferromagnetic ordering on details of the bonding angles and the lattice size. The effect of the cell decrease on the magnetic properties induced by substituting Eu for Ce appears to be rather indirect via a systematic change of Cr - O - Cr bonding and torsion angles which become necessary in order to accommodate

the rather rigid CrO_6 octahedra in the shrinking lattice. Substituting Eu for Ce in Ce orthochromites of composition $\text{Ce}_{1-x}\text{Eu}_x\text{CrO}_3$ not only rapidly decreases the Néel temperature of the antiferromagnetic ordering of the Cr^{3+} moments, but also gradually changes the thermal hysteresis behavior observed in the dc magnetization. In fact, samples with higher Eu content show a ZFC/FC splitting with a small peak in the FC susceptibility whereas the FC magnetization is reminiscent of the development of spontaneous magnetization in a ferromagnet. However, the saturation magnetization is far too low to account for the expected saturation magnetization of $\sim 3\mu_B$ expected for Cr^{3+} with the spin $S=3/2$ moment. This finding rather indicates canted antiferromagnets as found e.g. for EuCrO_3 .¹⁶ Using high-resolution x-ray diffraction measurements with sufficient intensity up to d -values of $\sim 0.4 \text{ \AA}$ allowed us to reliably refine oxygen atom positions. From our structural investigation we concluded: (a) The cell volume decreases by $\sim 2.5\%$ from CeCrO_3 to EuCrO_3 implying an overall increased density of Cr cations per unit volume for increasing Eu content. (b) Even though the cell volume reduction implies an overall increased density of Cr cations per unit volume, the Néel temperature decreases linearly with the Eu content. Figure 14 showing the Néel transition temperature of $\text{Ce}_{1-x}\text{Eu}_x\text{CrO}_3$ versus Eu content summarizes the results of all magnetic characterization measurements performed on the various phases studied in this work.

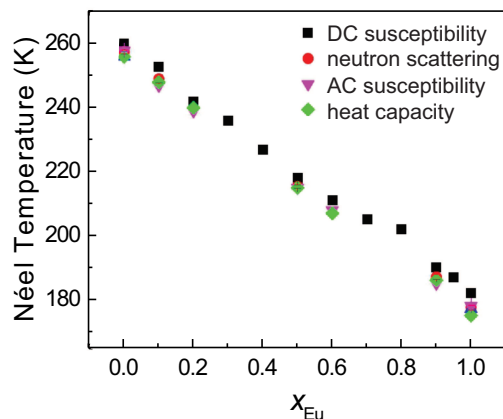


FIG. 14. (color online) Néel transition temperature (T_N) versus europium concentration, x , in $\text{Ce}_{1-x}\text{Eu}_x\text{CrO}_3$, obtained from the different techniques used in this work.

The Néel temperatures decrease linearly with the Eu content following a Vegard's-type dependence on the Eu concentration according to

$$T_N = 260K - x \times 80K.$$

An analogous decrease of T_N induced by a decreasing cell volume across the whole series of the rare earth

orthochromites has been observed before.^{12,14} From the light to the heavier rare-earth elements T_N of RCrO_3 decreases by 60%. In terms of lanthanide contraction, the solid-solutions investigated in this work cover approximately half of the rare-earth series. By adjusting the Ce/Eu ratio, they allow to divide the interval between CeCrO_3 and EuCrO_3 into several small intervals which enables us to relate T_N with minute structural changes. Substituting Ce by the smaller Eu cations exerts chemical pressure. Using first-principles calculations Zhao *et al.* have estimated the effects of chemical pressure external versus hydrostatic pressure on the Néel temperature of rare-earth orthochromites.¹⁸ They found that hydrostatic pressure essentially modifies bond distances and in turn leads to an increase of the Néel temperature whereas chemical pressure exerted by substituting a smaller rare-earth cation reduces the Néel temperatures by modifying antipolar displacements, Cr - O - Cr bond angles and the resulting oxygen octahedral tilts.¹⁸

(c) Despite the decrease of the cell volume, the CrO_6 octahedra did neither shrink nor distort significantly. The Cr - O1 distances remain almost constant (cf. Fig. 10(a)) and one does not expect a marked alteration of the energies of the t_{2g} orbitals. The Cr - O2 distances (cf. Fig. 10(b) and (c)) exhibit a slight opposite dependence on the Eu content, however, their mean value exhibits only a very small, approximately linear increase by less than a percent. Accordingly, the "skewness" of the octahedra remains below $\sim 2^\circ$ (cf. Fig. 8).

(d), Most striking, however, are the changes of the oxygen positions in the cell and the Cr - O - Cr bonding and torsion angles. The O1 atoms move considerably into the direction of the c - axis ($\sim 5\%$, cf. Fig. 7(a)). Apparently, as a consequence of the decrease of the cell parameters and the cell volume and in order to keep the shape and size of the CrO_6 octahedra essentially unchanged, the Cr - O2 - Cr bonding angles decrease by $\sim 6\%$ (cf. Figure 9(a)). Simultaneously, the torsion angle O1 - Cr - Cr - O1 which measures to what extent neighboring CrO_6 octahedra are inclined with respect to each other increases by $\sim 25\%$ (cf. Figure 9(a)). The importance of bonding angles for the superexchange and the magnetic ordering has been investigated in detail by Zhou *et al.* for the RCrO_3 phases with emphasis on the heavy rare-earth elements and some light rare-earth $R = \text{La}, \text{Pr}, \text{Nd}$. In our investigation we have divided the range from CeCrO_3 to EuCrO_3 , i.e. starting from a rare-earth element with a rather large ionic radius into several intervals and find analogous relationships between magnetic ordering and bonding and torsion angles. Especially the latter has been identified to be very essential for intrasite hybridization between Cr t and e orbitals. Intrasite hybridization lifts the t degeneracy and supports ferromagnetic coupling versus antiferromagnetic superexchange between the Cr - Cr moments.¹²

Finally we want to briefly comment on the crossing of the lattice parameters a and c (Figure 5) and the behavior of the positional parameters z_{O1} and x_{O1} of the

apical oxygen atoms (Figure 7) being different for small Eu levels, $x \leq 0.04$ from the behavior for $x \geq 0.3$. The intersection of a and b near $x = 0.04$ also reflected by the very small cell distortion factor (Figure 6) pointing to a lattice metrics close to cubic, seemingly indicating an attractive energy minimum which also pins the O1 atom positional parameters. Alternatively, a relaxation of lattice strain in the vicinity of the cubic metrics by random substitution of a substantially smaller Eu cation may also be taken into consideration to explain this observation.

In summary, our highly resolved x-ray powder and neutron powder diffraction measurements reveal that in the solid solutions $\text{Ce}_{1-x}\text{Eu}_x\text{CrO}_3$ the CrO_6 octahedra remain essentially rigid whereas Cr - O bonding and torsion angles change markedly by gradually substituting Ce by Eu. Simultaneously, the Néel temperature decreases from 260 K to 180 K. As the O2 - Cr - O2 bonding angle continuously moves away from 180° the torsion angles, which reflects to what extent the Cr - O2 - Cr bonds ro-

tate out of the $a - c$ plane when the size of the rare-earth ion is gradually reduced. This appears to constitute another determining parameter for magnetic ordering in the solid-solution phases $\text{Ce}_{1-x}\text{Eu}_x\text{CrO}_3$.

[†] Present address: Department of Chemistry, University of Calgary, Calgary, Canada.

[‡] Present address: Santa Clara University, Physics Department, 500 El Camino Real Santa Clara, CA 95053

ACKNOWLEDGMENT

This research was financially supported by Brock University, the Natural Sciences and Engineering Research Council of Canada (NSERC), the Ministry of Research and Innovation (Ontario), and the Canada Foundation for Innovation, Canada.

-
- ¹ J. I. R. Sahu, C. R. Serrao, N. Ray, U. V. Waghmare, and C. N. R. Rao, *J. Mater. Chem.*, **17**, 42 (2007).
 - ² B. Rajeswaran, D. I. Khomskii, A. K. Zvezdin, C. N. R. Rao, and A. Sundaresan, *Phys. Rev. B*, **86**, 214409 (2012).
 - ³ B. Raveau and M. M. Seikh, *Z. Anorg. Allg. Chem.*, **640**, 2649 (2014).
 - ⁴ R. Saha, A. Sundaresan, and C. N. R. Rao, *Mater. Horiz.*, **1**, 20 (2014).
 - ⁵ K. R. S. PreethiMeher, A. Wahl, A. Maignan, C. Martin, and O. I. Lebedev, *Phys. Rev. B*, **89**, 144401 (2014).
 - ⁶ A. McDannald, L. Kuna, M. S. Seehra, and M. Jain, *Phys. Rev. B* **91**, 224415 (2015).
 - ⁷ H. B. Lal, K. Gaur, R. D. Dwivedy, and N. Srivastava, *J. Mat. Sci. Lett.* **8**, 1434 (1989).
 - ⁸ A. Ghosh1, K. Dey, M. Chakraborty, S. Majumdar, and S. Giri, *EPL*, **107**, 47012 (2014).
 - ⁹ A. Ghosh, A. Pal, K. Dey, S. Majumdar, and S. Giri, *J. Mater. Chem. C*, **3**, 4162 (2015).
 - ¹⁰ C. M. N. Kumar, Y. Xiao, H. S. Nair, J. Voigt, B. Schmitz, T. Chatterji, N. H. Jalarvo, Th. Brückel, arXiv:1609.00928v1.
 - ¹¹ Xiangang Wan, Hang-Chen Ding, S. Y. Savrasov, and Chun-Gang Duan, *Scientific Reports* **6**, 22743 (2016).
 - ¹² J. S. Zhou, J. A. Alonso, V. Pomjakushin, J. B. Goodenough, Y. Ren, J. Q. Yan, and J.G. Cheng, *PHys. Rev. B* **81**, 214115, (2010)
 - ¹³ R. M. Hornreich, *J. Mag. Mag. Mater.*, **7**, 280 (1978).
 - ¹⁴ J. Prado-Gonjal, R. Schmidt, J. J. Romero, D. Ávila, U. Amador, and E. Morán, *Inorg. Chem.*, **52**, 313 (2013).
 - ¹⁵ R. Shukla, A. K. Bera, S. M. Yusuf, S. K. Deshpande. A. K. Tyagi, W. Hermes, M. Eul, and R. Pöttgen, *J. Phys. Chem. C*, **113**, 12663 (2009).
 - ¹⁶ M. Taheri, F. S. Razavi, Z. Yamani, R. Flacau, P. G. Reuvekamp, A. Schulz, and R. K. Kremer, *Phys. Rev. B*, **93**, 104414, (2016).
 - ¹⁷ Venkata Srinu Bhadrani, Diptikanta Swain, R. Dhanya, A. Sundaresan, and Chandrabhas Narayana, *Mater. Res. Express*, **1** (2014) 026111.
 - ¹⁸ H.J. Zhao, W. Ren, X. M. Chen and L. Bellaiche, *J. Phys: Condens. Matter*, **25**, 385604, (2013).
 - ¹⁹ S. Sasaki, C. T. Prewitt, A. C. Liebermann, *Am. Miner.* **68**, 1189 (1983).
 - ²⁰ M. Taheri, S. Trudel, R. K. Kremer, and F. S. Razavi, *J. Appl. Phys.*, **118**, 124306 (2015).
 - ²¹ R. D. Shannon, *Acta Cryst.*, **32**, 751 (1976).
 - ²² K. Tsushima, I. Takemura, S. Osaka, *Solid State Commun.*, **7**, 71 (1969).
 - ²³ M. Taheri, PhD Thesis, Brock University, (2016).
 - ²⁴ H. M. Rietveld, *J. Appl. Cryst.* **2**, 65 (1969).
 - ²⁵ J. Rodríguez-Carvajal, *Physica (Amsterdam)*, **192B**, 55. (1993).
 - ²⁶ TOPAS-Academic V6, by Coelho Software, Brisbane, Australia.
 - ²⁷ D. H. Ryan and L. M. D. Cranswick, *J. Appl. Cryst.*, **41**, 198 (2008).
 - ²⁸ M. Taheri, M. Konuma, and F. S. Razavi, *J. Surf. Interface Anal.*, DOI: 10.1002/sia.6069 (2016).
 - ²⁹ V. S. Bhadrani, B. Rajeswaran, A. Sundaresan, and C. Narayana, *Eur. Phys. Lett.* **101**, 17008 (2013).
 - ³⁰ A. Jaiswal, R. Das, S. Adyanthaya, P. Poddar, *J. Nanopart. Res.*, **13**, 1019-1027, (2011)
 - ³¹ Y. Su, J. Zhang, Z. Feng, Z. Li, Y. Shen. S. Cao, *J. Rare Earths.*, **29**, 1060, (2011)
 - ³² Y. Cao, S. Cao, W. Ren, Z. Feng, S. Yuan, B. Kang, B. Lu, and J. Zhang, *Appl. Phys. Lett.* **104**, 232405, (2014)
 - ³³ Structural parameters according taken from J. Prado-Gonjal, R. Schmidt, J. J. Romero, D. Ávila, U. Amador, and E. Morán, *Inorg. Chem.*, **52**, 313 (2013) given in cif file 251088.
 - ³⁴ K Yoshii, *Appl. Phys. Lett.*, **99**, 142501, (2011)
 - ³⁵ B. Tiwari, M. K. Surendra, M. S. R. Rao, *Materials Research Express*, **1**(3), 036102, (2014)
 - ³⁶ H. Satoh, S. Koseki, M. Takagi, W. Y. Chung, and N. Kamegashira, *J. Alloys Comp.*, **259**, 176 (1997).
 - ³⁷ F. Bartolomé, J. Bartolomé, M. Castro, J. J. Melero, *Phys. Rev. B*, **62**, 1058 (2000).

- ³⁸ Y. Su, J. Zhang, Z. Feng, L. Li, B. Li, Y. Zhou, Z. Chen, and S. Cao, *J. Appl. Phys.*, **108**, 013905 (2010).
- ³⁹ Y. Su, J. Zhang, Z. Feng, Z. Li, Y. Shen, and S. Cao, *J. Rare Earths*, **29**, 1060 (2011).
- ⁴⁰ M. Bouvier, P. Lethuillier, D. Schmitt, *Phys. Rev. B*, **43**, 13137 (1991).